A study of advanced high-loaded transonic turbine airfoils

Toyotaka Sonoda, Toshiyuki Arima, Markus Olhofer, Bernhard Sendhoff, Friedrich Kost, Peter Giess

2006

Preprint:

This is an accepted article published in Journal of Turbomachinery. The final authenticated version is available online at: https://doi.org/[DOI not available]

A STUDY OF ADVANCED HIGH LOADED TRANSONIC TURBINE AIRFOILS

Toyotaka Sonoda

Honda R&D Co. Ltd., Wako Nishi R&D Center

Saitama 351-0193, Japan

Toshiyuki Arima

Honda R&D Co. Ltd., Wako Research Center

Saitama 351-0193, Japan

Markus Olhofer **Bernhard Sendhoff**

Honda Research Institute Europe GmbH

63073 Offenbach, Germany

Friedrich Kost **P.-A. Giess**

Institute of Propulsion Technology

German Aerospace Center (DLR)

D-37073 Goettingen, Germany

ABSTRACT

The development of high performance turbine airfoils has been investigated under the condition of a supersonic exit Mach number. In order to obtain a new aerodynamic design concept for a high loaded turbine rotor blade, we employed an evolutionary algorithm for numerical optimization. The target of the optimization method, which is called evolutionary strategy (ES), was the minimization of the total pressure loss and the deviation angle. The optimization process includes the representation of the airfoil geometry, the generation of the grid for a blade-to-blade CFD analysis, and a 2D Navier-Stokes solver with a low-Re k-ε turbulence model in order to evaluate the performance. Some interesting aspects, for example, a double shock system, an early transition and a re-distribution of aerodynamic loading on blade surface, observed in the optimized airfoil, are discussed. The increased performance of the optimized blade has been confirmed by detailed experimental investigation, using conventional probes, hot-films and L2F system.

INTRODUCTION

The target of a blade designer for turbine and/or compressor airfoils in gas turbine engines is to produce blade shapes that have low losses at the design flow conditions. Furthermore, minimal losses also should also be obtained for a wide range of blade operating conditions, like incidence, Mach number and Reynolds number.

In general, turbine airfoils have very thick, blunt trailing edges, as compared with those of compressor airfoils. In subsonic flow the trailing edge loss of the turbine airfoil is usually small compared to the boundary layer losses and it is often neglected for airfoils with thin trailing edges. However, it is well known that with increasing exit Mach number toward unity, the loss coefficient rises sharply and the base pressure falls together with the complex shock pattern formed around the trailing edge (Sieverding et al., 1983). The loss usually continues to rise with the Mach number for low supersonic flow, but may level off and decrease at high exit Mach numbers for some type of blades (Graham and Kost, 1979). It is also known that the trailing edge loss increases roughly linearly with trailing edge blockage and as a result becomes more important for thick trailing edges and/or high solidity blades, like a hub section in rotor blades.

The pressure side shock just downstream of the trailing edge will propagate toward the suction surface of the adjacent blade and may have a large effect on its pressure distribution and on the loss due to the shock-boundary layer interaction together with two reflected shocks through the generation of a separation bubble (Stanewsky, 1973). The generation of the bubble seems to be strongly related to the boundary layer property just upstream of the interaction

point (Graham and Kost, 1979, and Dietrichs et al., 1987). Also, the suction side shock may lead to a strong distortion of the static pressure for a downstream cascade.

Although the *basic* flow pattern of the transonic turbine is well understood, it is interesting and challenging to develop a new design concept for the further advancement of high loaded transonic turbine airfoils. One approach to find new design concepts is to use modern numerical, global optimization techniques like evolutionary computation. The advantages of these methods are that they are able to identify a search direction in the huge parameter space, that they are able to escape local optima, that they do not require an analytical quality function and that they can operate successfully on noisy quality functions. Evolutionary algorithms have also been shown to produce robust solutions, i.e., solutions whose performance does not or only slightly deteriorate for variations of design conditions. Some papers on the 2D optimization of compressor airfoils have been published (Koeller et al., 2000, and Sonoda et al., 2003). However, hardly any literature can be found on the optimization of 2D turbine cascades. Shelton et al. (1993) minimized the downstream shock strength in order to generate a more homogeneous flow field in the downstream blade row. However, the total pressure loss for the optimized airfoil is about 25% greater than the loss for the baseline airfoil, although the suction side shock strength is reduced as compared to the baseline case. Furthermore, their emphasis in the paper is on the application of their optimization techniques rather than on the physical details of the resulting blade design.

In this paper, we discuss the optimization results of the evolutionary strategy applied to a rotor hub-section with a high trailing edge blockage for a high loaded single stage turbine. The baseline airfoil cross-section used in this research and the design parameters are shown in **Fig. 1** and **Table 1**.

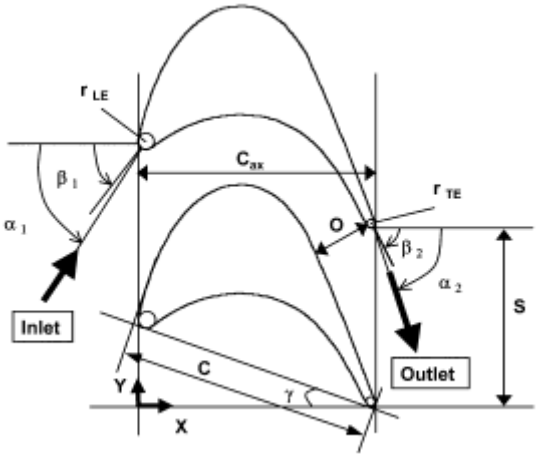

Fig. 1 Baseline airfoil geometry and cascade parameters

Table 1 Design parameters of baseline (HL) cascade

Aerodynamics		Geometry	
Ma_{2is}	1.2	C (mm)	60
α_2 (deg)	70	C_{ax} (mm)	55.687
α_1 (deg)	65	β_1 (deg)	58
Turning angle (deg)	135	β_2 (deg)	66.51
		γ (deg)	19.3
		C / S	1.413
AVDR	1.0	r_{TE} / C (%)	1.76
Re_2	$\approx 9 \times 10^5$	$2r_{TE}$ / O (%)	15.4

This airfoil is designated the baseline HL airfoil. The design outlet isentropic Mach number is 1.20 and the design outlet angle is 70 degrees. The flow turning angle is 135 degrees. The solidity and the throat blockage are about 1.4

and about 16% respectively. They are higher than previously published ones (Michelassi et al., 1997, and Jouini et al., 2001). The objective of the presented paper is to demonstrate the superior performance of the optimized turbine airfoils and to elucidate the reason of the higher performance, for which both extensive experimental tests as well as high precision CFD analysis are discussed.

NOMENCLATURE

AVDR	axial velocity density ratio: $AVDR = (\rho_2 u_2) / (\rho_1 u_1)$
C	chord length
CFD	computational fluid dynamics
E_M	time-averaged hot-film voltage with flow
$E0_M$	time-averaged hot-film voltage without flow
EXP	experiment
k	turbulent kinetic energy
Ma	Mach number
O	throat length
p	pressure
PS	pressure side
Re	Reynolds number based on chord length

RMS	root-mean-square of hot-film voltage
r	radius
S	pitch length
SS	suction side
u	velocity
X	axial-chord-wise location
Y	pitch-wise location
y^+	dimensionless distance from wall
α	flow angle
β	airfoil metal angle
γ	stagger angle
δ	boundary layer thickness
$\delta\alpha$	tolerance for exit flow angle
ε	turbulent kinetic energy dissipation
μ, λ	population size (parent, offspring)
ρ	density
ω	total pressure loss coefficient: $\omega = (p_{t1} - p_t)/p_{t1}$

Subscripts

1	inlet plane upstream of leading edge
2	exit plane downstream of trailing edge
ax	axial direction
design	target values for optimization
is	isentropic entity
LE	leading edge
TE	trailing edge
t	total

DESIGN APPROACH

The Evolutionary Algorithm

Evolutionary Algorithms belong to the class of global stochastic optimization algorithms. They are inspired by the principles of biological evolution and are based on a cyclic (generational) organization of the processes of reproduction, variation and selection in a population of individuals, i.e., here designs of a blade shape.

In this paper, we use a special type of evolutionary algorithms called evolutionary strategy, where the process of variation is realized by adding normally distributed random numbers to the parameters that define the blade shape. Starting from a so called parent population, offsprings are generated by randomly choosing individuals from the parent population and copying them to the offspring population until all λ individuals in this population are initialized. Thereafter, a normally distributed random vector is added to the parameter set of all offsprings, which are evaluated. Finally, the best μ individuals are selected to form the parent population of the following generation. The standard deviation of the normal distribution controls the width of the search and is itself subject to variations during the search. This principle of adaptation of the search width to the topology of the search space is referred to as *self-adaptation*. In this paper, we use the CMA (Covariance Matrix Adaptation) method (Hansen and Ostermeier, 2001) for which the full covariance matrix of the normally distributed random vector is adapted. This allows the adaptation of the search direction independently from the chosen coordinate system of the search space, in other words correlations between design parameters can be taken into account during the search process. This method is

known to have a high convergence rate resulting in a reasonable overall calculation time. The presented blade geometry is the result of a strategy with $\mu = 1$ parent individual and $\lambda = 12$ offspring individuals in each population.

The Blade Profile Definition

We encode the blade cross-section by a 3rd order B-spline. The control points and the resulting curve that represents the cross section of the blade are shown in **Fig. 2**.

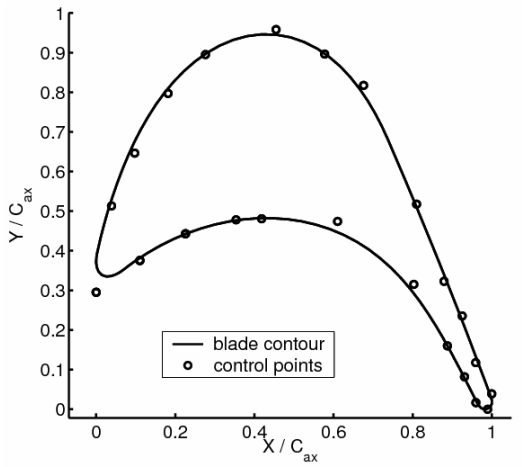

Fig.2 B-spline and initial blade

The circles show the control points of the 3rd order B-spline; the solid line shows the resulting spline that describes the cross-section of the blade. The number of control points is fixed to p=23 points. Each point is represented by its Cartesian coordinates. The dimension of the resulting parameter set, which is optimized, is therefore n = 46. The initial set of control points for both optimizations is shown in **Fig. 2**. The 46 design parameters are stored in a vector, which is called a chromosome of an individual in the context of evolutionary computation.

The Quality Function

In order to evaluate the quality of each set of 46 design parameters, the spline curve is built out of the control points in the first step. In the next step, the geometric properties of the described cross-section are calculated and used to determine whether the geometric constraints of the optimization are satisfied. Afterwards, the aerodynamic properties are calculated using the Navier-Stokes flow solver, see next section. The overall quality is then calculated by a weighted sum of the total pressure loss ω, the deviation of the outflow angle from the target angle and a penalty value in case the trailing edge thickness r_{TE} is below a given minimal value. Therefore, the overall quality value *f* is given by

$$f = \sum_{i=1}^{3} w_i t_i \rightarrow minimize,$$

where the w_i are weighting coefficients, which are fixed heuristically, and the t_i are given as follows:

$$t_1 = \max(0 \ , \ |\alpha_2 - \alpha_{2,design}| - \delta\alpha)$$
$$t_2 = \omega$$
$$t_3 = \max(0 \ , \ r_{TE,design} - r_{TE})$$

The target outflow angle is given by $\alpha_{2,design}$, the tolerance range for the deviation is $\delta\alpha = 0.3$ and the minimal allowed radius of the trailing edge is given by $r_{TE,design}$ = (0.0176 × *chord length).*

The result of the optimization after about 130 generations of the algorithm is shown in **Fig. 3**.

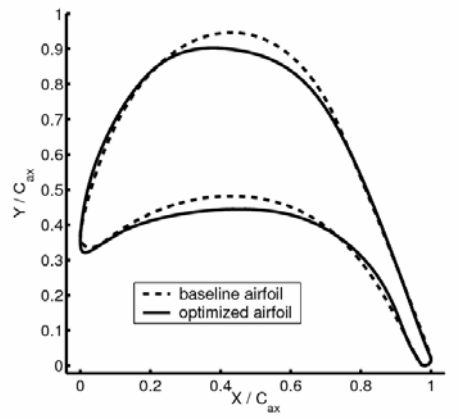

Fig. 3 Baseline (HL) and optimized (ES) airfoil geometries

The optimized airfoil will be denoted in the following by "Optimized ES" or in short by "ES". The stagger angle for the ES is slightly reduced by 1 degree and the maximum curvature point on the SS is significantly shifted toward the front side (from 40% to 25% of axial chord position). It is also interesting that the curvature around the middle part of the PS is slightly lower, while the shape between 75% and 90% of axial chord position is slightly indented (compared to the HL blade). We can see the locally high concave curvature near the trailing edge. A re-distribution of aerodynamic loading on the blade surface seems to be realized by the optimized ES airfoil.

The Navier-Stokes Solver

For the numerical analysis, a quasi-three-dimensional (Q3D) version of the Navier-Stokes flow solver HSTAR (Honda Software for Turbomachinery Aerodynamics Research) with a low Reynolds k-ε turbulence model proposed by Chien (1982) has been used. The HSTAR Q3D solver was developed by Honda R&D, it is a modified 3D Navier-Stokes code for the purpose of calculating the aerodynamic performance of 2D cascades (Arima et al., 1999). Two types of simulations were carried out. One for the evaluation of the airfoil geometries during the optimization

and one for the detailed analysis of the flow physics after optimization. The axial velocity density ratio (AVDR) is set to one for all computations. The computational grids used in analyzing the flow physics are shown in **Fig. 4**.

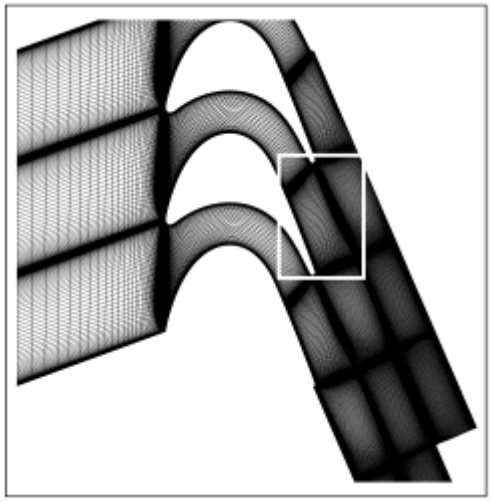

(a)

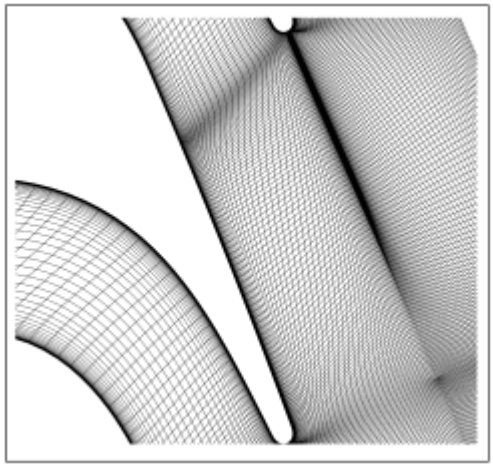

(b)

Fig. 4 Computational grid used in numerical analysis: (a) Overall; (b) Enlargement

The grid consists of 541×71 cells, which is much finer than the one used in the optimization process (191×55). The average y+ of the first grid point from the wall is about 0.5 for all calculations. In order to obtain a high resolution of the shock-boundary layer interaction, 200 cells are arranged on the suction surface and 100 cells on the pressure

surface. This cell arrangement results in grid orthogonality in the uncovered region which is an important requirement for a CFD grid for the analysis of shock boundary layer interaction.

EXPERIMENTAL APPROACH

The Windtunnel for Straight Cascades (EGG)

The experiments reported in this paper were performed in the wind-tunnel for straight cascades at DLR Goettingen. The facility is of the blow-down type with atmospheric inlet. Downstream of the cascade, the flow passes an adjustable diffuser and the main butterfly valve and finally enters a large vacuum vessel (10,000 m^3). The Reynolds number cannot be varied independently, but is a function of the Mach number which is set by the adjustable diffuser. The cascade is mounted between two circular disks establishing the side walls of the flow channel. The inlet angle is adjusted by turning this assembly. The test section dimensions are (380×125) mm^2, which allowed the cascade of the present tests to consist of 15 blades. The installed cascade had at least 14 blades within the flow. The periodicity was checked for 10 pitches in subsonic flow and for 6 pitches at design Mach number of 1.2. A good periodicity has been achieved for all these measurements. Therefore, the wake measurements for the optimization condition were carried out over 3 pitches. For more details on the windtunnel set-up, the interested reader is referred to http://www.dlr.de/EN-AT.

The Surface Pressure and Probe Measurements

For surface pressure distribution measurements one of the blades mounted in the cascade centre was substituted by an instrumented blade equipped with 30 pressure tappings. In order to determine the performance of the cascade, the wake flow was measured by traversing a wedge type probe far behind the cascade. From the data on the local inhomogeneous flow in the traverse plane, the properties of the equivalent homogeneous (mixed out) outlet flow are obtained by applying the equations of conservation of mass, momentum and energy (Amecke and Safarik, 1995). Inside the blade channels a flattened Pitot probe was used with a probe head size of 0.25mm × 1mm, enabling measurements in the boundary layers close to the blade surface. The measurement planes are shown in **Fig. 5**.

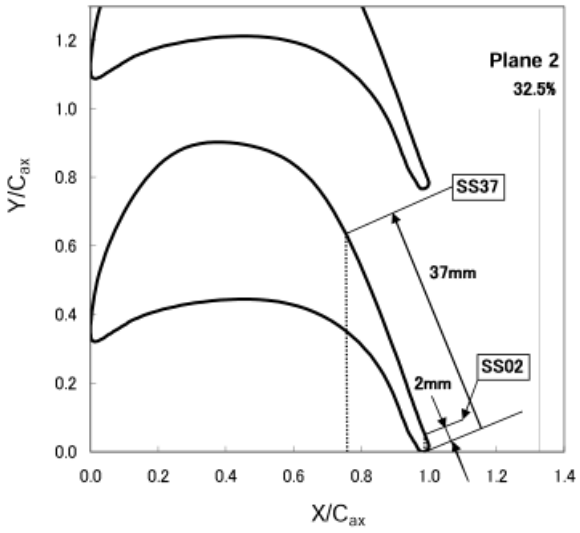

Fig. 5 Measurement planes inside cascade and downstream

In the case of laser velocimetry by L2F and Pitot-pressure measurements in the same plane, the L2F results (local Mach number and flow angle) and the Pitot pressure could be combined to obtain local flow data in the same way as from the wedge probe. Whereas, due to the size of the probe, reliable wedge probe measurements could be performed

only further downstream, the combination of L2F and Pitot pressure measurements allowed for investigations inside the cascade.

Pressures are measured with an accuracy of 0.1%, but to convert probe pressures into flow values a calibration is needed. Furthermore, the periodicity of the cascade flow suffers from reflected shocks in supersonic flow. Accordingly, the final accuracy of the measured flow data is only 1-2% for the Mach number and 0.5% for the loss.

The Laser-2-Focus Measurement Technique

The measurement principle of L2F is rather simple. The L2F-measuring device generates two highly focused light beams in the probe volume which act as a 'light gate' for tiny particles in the flow. The scattered light from the particles provides two successive pulses and from the time interval between the pulses the velocity perpendicular to the laser beams can be derived (Schodl, 1980). The two foci of the used L2F device have diameters of 8μm and their separation is 210.8μm. In order to increase the data rate, the flow has to be seeded. The necessary particles are oil droplets of 0.3μm diameter which are produced by a special seeding generator and injected into the flow in the settling chamber.

At DLR Goettingen the Laser-Two-Focus technique (L2F) is routinely applied to acquire flow field information for cascade and turbomachine flows (Kost and Kapteijin, 1997). The system measures 2D-vectors of the fluid velocity. The present laser measurements were analyzed and the experimental uncertainties (on a 95% confidence level) were determined: The error bar for the Mach number was 0.003 outside the wakes and 0.006 inside. The error bar for the flow angle was 0.2° outside the wake and 0.4° inside.

VALIDATION OF DESIGN AND DISCUSSION

This presentation of the experimental (EXP) and/or numerical results (CFD) concentrates on the transonic case with isentropic exit Mach number, Ma_{2is}=1.2, although a wide range of Mach numbers were investigated.

The Flow Pattern for Baseline (HL) and Optimized (ES)

A qualitative view of a two-dimensional transonic flow field can be gained by Schlieren pictures which visualize the density gradients. Schlieren photos make shocks, wakes and separation zones visible as well as regions of flow deceleration and acceleration. **Figure 6** displays the experimental/numerical flow fields of cascade HL.

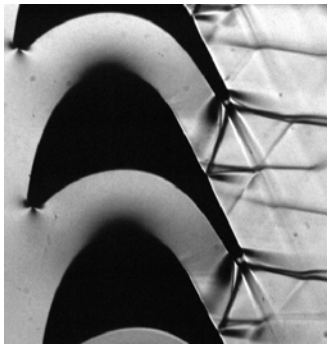

(a) EXP

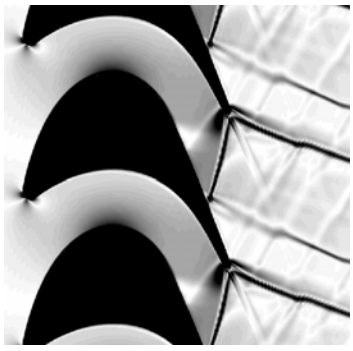

(b) CFD

Fig. 6 Schlieren photo of baseline cascade (HL) at Ma_{2is}=1.2, α_1=65°: (a) EXP; (b) CFD

In **Fig. 6 (a)**, i.e., for the HL experiment, the conventionally designed blade HL shows one shock originating at the trailing edge of the neighboring blade, which impinges onto the suction side and is reflected as two shocks. This is a strong indication that a rather long separation bubble has been caused by the impinging shock (Graham and Kost, 1979). **Figure 7** shows the experimentally observed separation bubble near the impingement and a schematic figure of shock/boundary layer interaction.

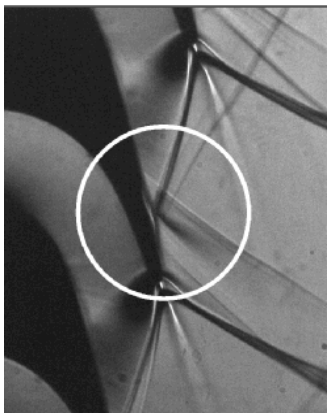

(a)

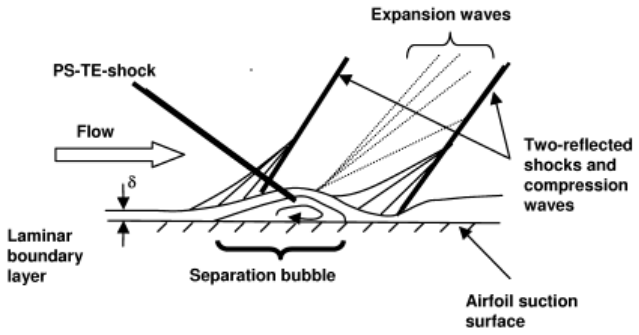

(b)

Fig. 7 Generation of separation bubble by a shock boundary layer interaction at Ma_{2is}=1.5, α_1=65°:

(a) Schlieren photo near impingement; (b) Schematic figure of a shock/boundary layer interaction

In order to better visualize the bubble (without changing the interaction), the Mach number for the Schlieren photo in Fig. 7(a) is higher than the one in Fig. 6(a). Such a long separation bubble may only exist if the upstream suction side boundary layer is still laminar. As shown in **Fig. 6 (b)**, CFD shows a similar pattern as EXP, but the two reflected shocks near the interaction point are not captured.

In the optimized airfoil (ES), an additional shock pattern is observed experimentally and numerically around just upstream of TE on the PS. Therefore, a double shock pattern is generated, as shown in **Figs. 8 (a) and (b)**.

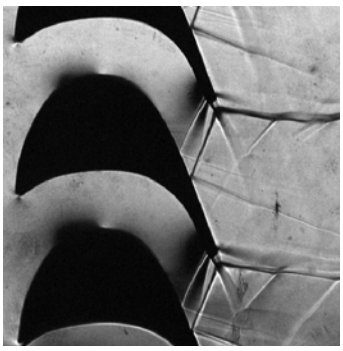

(a) EXP

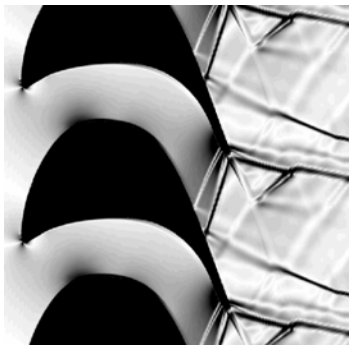

(b) CFD

Fig. 8 Schlieren photo of optimized cascade (ES) at Ma_{2is}=1.2, α_1=65°: (a) EXP; (b) CFD

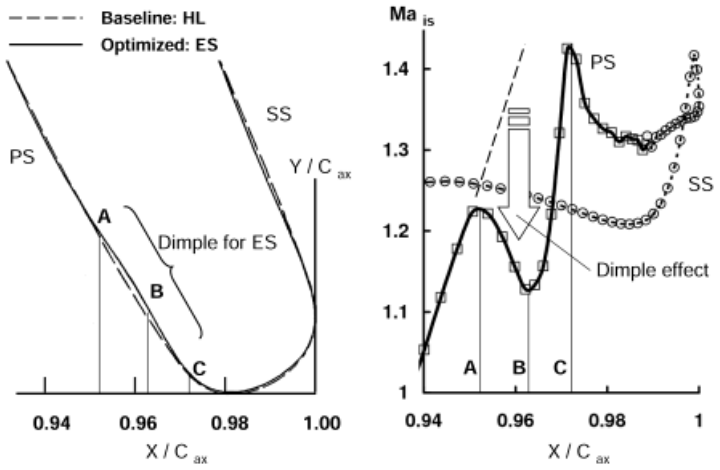

Fig. 9 Computed effect of dimple on airfoil surface Mach number distribution for optimized cascade (ES) at Ma_{2is}=1.2, α_1=65°

Figure 9 shows the reason why the second shock is induced for the optimized ES blade. There is a dimple near TE on PS. The depth of the dimple is very small (about 100 μm), while the manufacturing precision is about 20 μm. Due to the small dimple, the Mach number distribution near the TE on PS is significantly controlled to have a weaker TE-shock. That is, the continuous increase of Mach number toward the TE on PS is suppressed by the second shock that is generated around the dimple. Therefore, the Mach number from point A to point B is decreased. As a result, the absolute Mach number at point C, related to the strength of TE-shock on PS, is decreased. One of the design concepts of the ES blade is to produce such a double shock system or multi shock system just upstream of TE on PS. Additionally, there is a region of deceleration on the suction side upstream of the throat (the white patch on the uppermost part of the suction side contour in **Fig. 8 (a)**). The role of this "region of deceleration" will become clearer in Section "The Airfoil Surface Mach Number". Each shock impinging on the suction side gives rise to only one reflected shock, a clear hint that there is no separation bubble and that the boundary layer approaching the shock

ought to be turbulent. In CFD, the double shock system is also captured. Overall there is a good qualitative agreement between EXP and CFD, see **Fig. 8 (b)**.

The Airfoil Surface Mach Number

Figure 10 shows the airfoil surface Mach number distributions for HL and ES airfoils at the design inlet flow angle of 65 degrees.

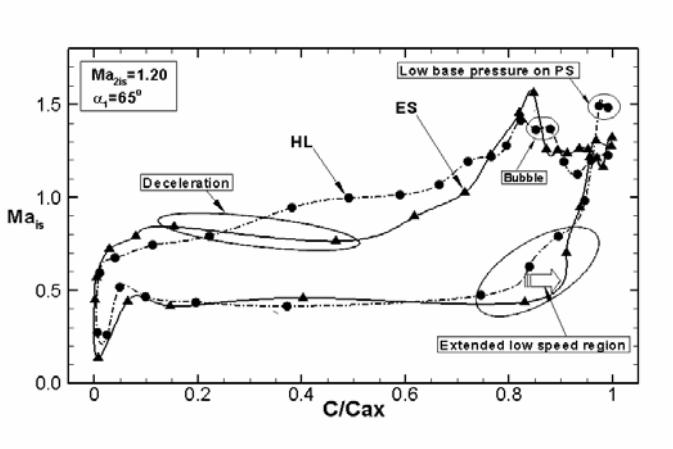

Fig. 10 Measured airfoil surface Mach number distribution for baseline (HL) and optimized (ES) at design conditions at Ma_{2is}=1.2, α_1=65°

There are four interesting points for the optimized airfoil. First, the ES blade has a decelerated region in the front part of SS, as already shown in **Fig. 8 (a)**. The gradient seems to be small, but the decelerated region can be clearly identified by coupling EXP with CFD, as shown in **Fig. 11**. This decelerated region may lead to an early boundary layer transition for the ES blade. Second, the bubble around 85% of axial chord for the HL blade cannot be observed for the optimized ES blade. Third, the ES blade has a smaller Mach number absolute level (i.e., higher base pressure) on the pressure surface near the trailing edge compared to the HL blade. This may lead to a small trailing edge loss as

well as to a weak shock generated at the pressure side just downstream of the trailing edge. Finally, a low speed region is significantly extended towards downstream on the pressure surface. This is due to the locally high concave curvature near the trailing edge, as already shown in **Fig. 3**.

Figure 11 shows the effect of the inlet flow angle on the surface Mach number distribution for both HL and ES airfoils, experimentally and numerically.

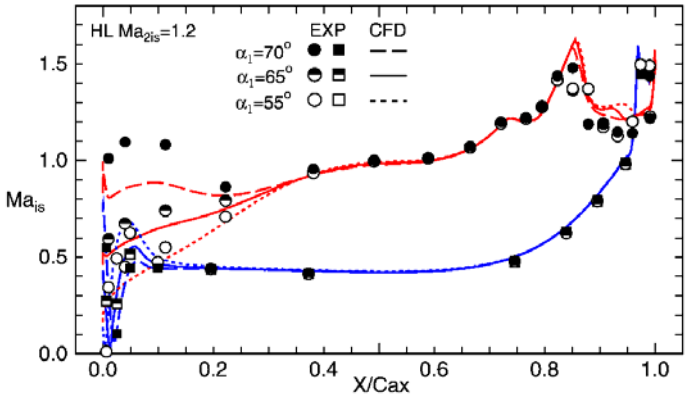

(a) Baseline (HL)

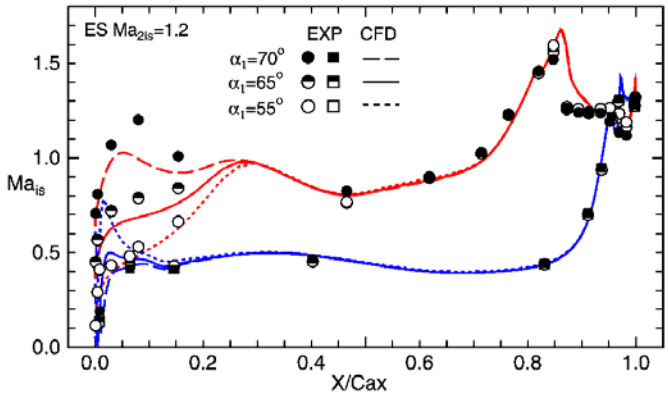

(b) Optimized (ES)

Fig. 11 Comparison of CFD with EXP for airfoil Mach number distribution at Ma_{2is}=1.2: (a) Baseline (HL); (b) Optimized (ES)

There is a reasonably large discrepancy in the front part of the airfoil between EXP and CFD. This is due to the difference of AVDR between EXP (AVDR≈ 0.90) and CFD (AVDR= 1.0). In the case of the ES blade, EXP and CFD clearly show the decelerated region from about 30% to 50% of chord length, as already described above. As a result, the boundary layer transition can be observed for the ES blade. Thus, there seems to be no bubble for three inlet flow angles. The clearer flow patterns around the uncovered region on SS for the HL and ES blades are shown in **Figs. 12 and 13**, respectively.

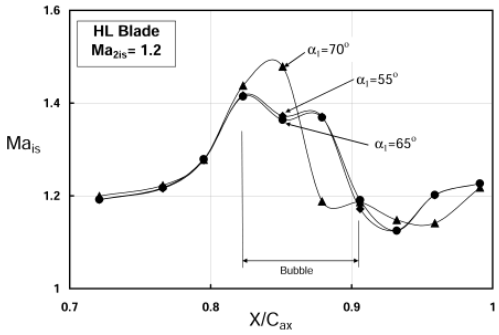

Fig. 12 Measured suction surface Mach number distribution around uncovered region for baseline HL airfoil at Ma_{2is}=1.2

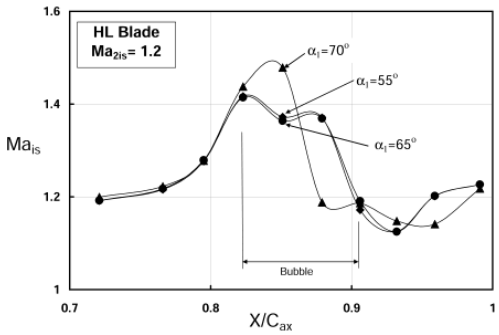

Fig. 13 Measured suction surface Mach number distribution around uncovered region for optimized ES airfoil at Ma_{2is}=1.2

We can see that there is a bubble between 85% and 90% of axial chord position for two inlet flow angles of 55 and 65 degrees for the HL blade. In the case of a very positive incidence angle (the inlet flow angle is 70 degrees) the boundary layer transition can be observed due to the high deceleration in the front part for the HL blade. In the case of the ES blade, the boundary layer is already turbulent (see **Fig. 13**).

The Boundary Layer Property

It is highly probable that the transition of the boundary layer on the suction side took place in the mentioned deceleration region of the ES blade. This can be confirmed by the results of hot-film measurements displayed in **Fig. 14**.

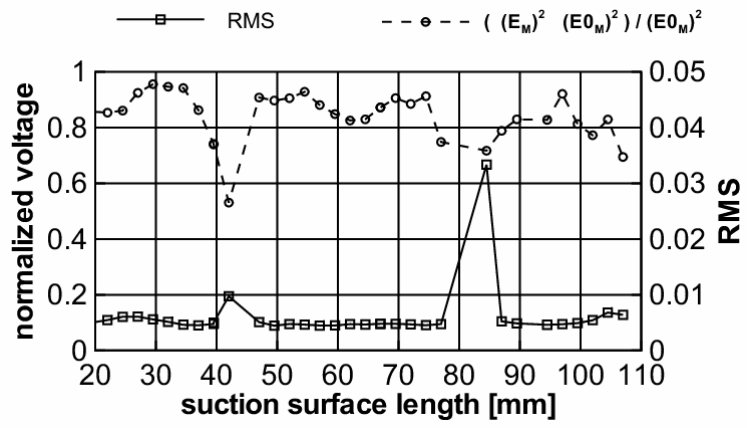

Fig. 14 Hot-film measurements along the suction surface of optimized ES airfoil at Ma_{2is} = 1.2, α_1 = 65°

Here the normalized (mean) voltage shows a deep depression at suction surface length 42mm and at the same position a peak can be observed in the RMS value. These features are the footprint of a separation bubble that causes the boundary layer transition. We also note that the second peak of the RMS value and the depression of voltage at

suction surface length 84mm mark the impingement of the main trailing edge shock onto the suction side of the ES blade.

These different features of the ES blade compared to the HL blade result in a different development of the blade boundary layers and accordingly in different friction losses. Because of the much higher velocity on the suction side compared to the pressure side, the losses are mainly generated at the suction side. At design Mach number, Ma_{2is}=1.2, the shock and the trailing edge losses should be already of more importance than the friction losses.

In **Table 2** a comparison of the measured boundary layer thicknesses at suction side is presented.

Table 2 Boundary layer thickness on SS at Ma_{2is}=1.2, α_1=65°

	X/Cax	δ (mm)	
		HL	ES
SS-37	0.759	0.211	0.820
SS-02	0.993	0.921	2.126

The two positions where results are shown are upstream of the shock impingement (SS-37) and 2mm upstream of the trailing edge (SS-02). We can briefly summarize the observations as follows: At both positions the HL blade clearly shows the thinner boundary layer and accordingly the lower friction loss. The same conclusion can be drawn from **Figs. 15 and 16** where the measured total pressure is displayed. In the vicinity of the suction side, the HL blade has a thinner boundary layer than the ES blade.

The Total Pressure Loss

In **Fig. 15,** the total pressure loss is close to zero outside the suction side boundary layer but rises sharply when approaching the wake (the plane SS-37 passes the trailing edge of the neighboring blade at a distance of 2mm).

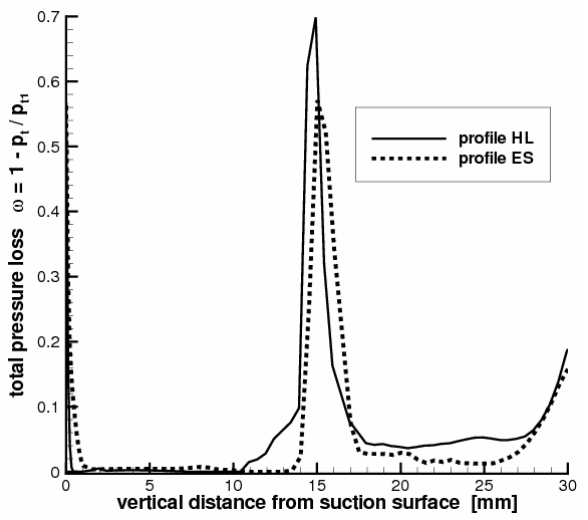

Fig. 15 Measured total pressure loss coefficient in plane SS-37 at Ma_{2is} = 1.2, α_1 = 65°, x/C_{ax} = 0.759

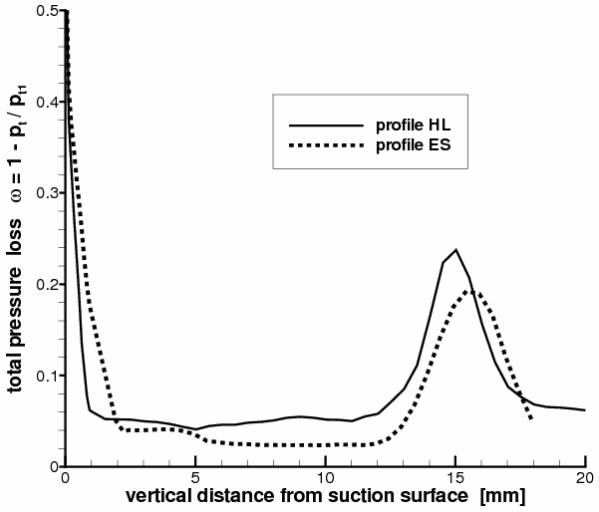

Fig. 16 Measured total pressure loss coefficient in plane SS-02 at Ma_{2is} = 1.2, α_1 = 65°, X/C_{ax}=0.993

Blade HL generates the bigger trailing edge loss compared to the ES cascade, although trailing edge thickness is very similar for the two blade geometries. This is probably due to the Mach number reduction (maybe the base pressure for the ES blade is increased) at the trailing edge on the pressure side, as already shown in **Fig. 10**. This is related to the trailing edge of the ES blade: “a locally high concave curvature” and “a small dimple”, as shown in **Fig. 3** and **Fig. 9**, respectively. These specific shape properties have a positive influence. The total pressure loss from plane SS-37 to plane SS-02 (**Fig. 16**) between boundary layer edge and wake is caused by the shocks. Comparing these shock losses the HL cascade is worse than the ES cascade. The results of plane SS-02 further confirm that the trailing edge loss is bigger for the HL blade.

The mixed out flow losses downstream of the cascades were obtained from the wedge probe measurements. Therefore, they are independent of the measurements shown in the upper figures. The energy loss is derived from enthalpy and defined according to Horlock (1966). The results show that the energy loss of the ES cascade is smaller than the one of the baseline HL cascade. The improvement is about 12% (not shown here) at Ma_{2is}=1.2.

CONCLUSIONS

An evolutionary optimization method, namely evolutionary strategy, was applied to the design of a high turning transonic turbine airfoil at supersonic exit Mach number of 1.20 together with a Navier-Stokes solver with Chien’s low Reynolds k-ε turbulence model. Furthermore, the aerodynamic characteristics for the baseline airfoil called HL

and the optimized airfoil called ES were analyzed numerically as well as experimentally. The following conclusions can be drawn.

1. The superior performance of the optimized airfoil with 12% of energy loss reduction is gained at design exit isentropic Mach number of 1.2.

2. For the optimized airfoil, the trailing edge loss and the shock loss are improved, although the friction loss is worse than for the baseline. This means that the shock and trailing edge losses should be of higher importance than the friction loss in transonic turbine cascades. From the optimization point of view it might also indicate that there is a trade-off between friction and shock/trailing edge loss.

3. The improvements of the trailing edge loss and shock loss are due to the reduction of the Mach number on the pressure side near the trailing edge. This is achieved by special geometric properties of the optimized blade: “a locally high concave curvature” and “a small dimple” on the pressure surface near the trailing edge. These properties lead to a “double shock system” and increase the base pressure.

4. In the case of the optimized airfoil, the boundary layer just upstream of the shock/boundary layer interaction point on the suction surface is fully turbulent due to a deceleration region of the front part of the airfoil. Therefore, no separation bubble is observed for three inlet flow angles, while in the case of the baseline airfoil, the separation bubble is observed for all inlet flow angles, except for an extreme positive flow angle of 70 degrees.

REFERENCES

[1] Sieverding, C.H., Stanislas, M., and Snoek, J., 1983, "The BASE Pressure Problem in Transonic Cascades," ASME Paper No. 83-GT-50.

[2] Graham, C.G., and Kost, F.H., 1979, "Shock Boundary Layer Interaction on High Turning Transonic Turbine Cascades," ASME Paper No. 79-GT-37.

[3] Stanewsky, E., 1973, "Shock Boundary Layer Interaction in Transonic and Supersonic Flow," Lecture Series 59 "Transonic Flow in Turbo-machines," von Karman Institute, Brussel.

[4] Dietrichs, H.-J., Hourmouziadis, J., Malzacher, F., and Braeunling, W., 1987, "Flow Phenomena in Transonic Turbine Cascades; Detailed Experimental and Numerical Investigation," ISABE 87-7031.

[5] Koeller, U., Moenig, R., Kuesters, B., and Schreiber, H.A., 2000, "Development of Advanced Compressor Airfoils for Heavy-Duty Gas Turbines, Part 1: Design and Optimization," ASME *Journal of Turbomachinery*, Vol. 122, pp. 397-405.

[6] Sonoda, T., Yamaguchi, Y., Arima, T., Olhofer, M., Sendhoff, B., and Schreiber, H. A., 2004, "Advanced High Turning Compressor Airfoils for Low Reynolds Number Condition, Part 1: Design and Optimization", ASME *Journal of Turbomachinery*, Vol. 126, No. 3, pp. 350-359.

[7] Shelton, M.L., Gregory, B.A., Lamson, S.H., Moses, H.L., Doughty, R.L., and Kiss, T., 1993, "Optimization of a Transonic Turbine Airfoil using Artificial Intelligence, CFD and Cascade Testing," ASME Paper No. 93-GT-161.

[8] Michelassi, V., Rodi, W., and Giess, P.-A., 1997, "Experimental and Numerical Investigation of Boundary-Layer and Wake Development in A Transonic Turbine Cascade," ASME Paper 97-GT-483.

[9] Jouini, D.B.M., Sjolander, S.A., and Moustapha, S.H., 2001, "Midspan Flow-Field Measurements for Two Transonic Linear Turbine Cascades at Off-Design Conditions," ASME Paper No. 2001-GT-0493.

[10] Hansen, N., and Ostermeier, A., 2001, "Completely Derandomized Self-Adaptation in Evolution Strategies," *Evolutionary Computation*, Vol. 9, No. 2, pp. 159-196.

[11] Chien, J. Y., 1982, "Predictions of Channel and Boundary Layers With a Low-Reynolds-Number Two Equation Model of Turbulence," AIAA *Journal*, Vol. 20, pp. 33-38.

[12] Arima, T., Sonoda, T., Shirotori, M., Tamura, A., and Kikuchi, K., 1999, "A Numerical Investigation of Transonic Axial Compressor Rotor Flow Using a Low-Reynolds-Number k-ε Turbulence Model," ASME *Journal of Turbomachinery*, Vol. 121, pp.44-58.

[13] Amecke, J., and Safarik, P., 1995, "Data Reduction of Wake Flow Measurements with Injection of an Other Gas", Forschungsbericht DLR-FB 95-32, Cologne.

[14] Schodl, R., 1980, “A Laser-Two-Focus (L2F) Velocimeter for Automatic Flow Vector Measurements in the Rotating Components of Turbomachines,” *Journal Fluids Engineering*, Vol. 102, pp. 412-419.

[15] Kost, F., and Kapteijn, C., 1997, “Application of Laser-Two-Focus Velocimetry to Transonic Turbine Flows,” Proc. 7th International Conference on Laser Anemometry - Advances and Applications, University of Karlsruhe, Germany.

[16] Horlock, J.H., 1966, “Axial Flow Turbines,” Robert E. Krieger Publishing Company, Malabar, USA